Distribution of shear force in perforated shear connectors

Xing Wei [1a], M. Shariati [*2,6], Y. Zandi [**3], Shiling Pei [1b], Zhibin Jin [4c],
S. Gharachurlu [3d], M.M. Abdullahi [5e], M.M. Tahir [6f] and M. Khorami [7g]

[1] *Department of Bridge Engineering, School of Civil Engineering, Southwest Jiaotong University, Chengdu 610031, China*
[2] *Faculty of Civil Engineering, University of Tabriz, Tabriz, Iran*
[3] *Department of Civil Engineering, Islamic Azad University, Tabriz Branch, Tabriz, Iran*
[4] *Department of Civil and Environmental Engineering, Colorado School of Mines, Golden, USA*
[5] *Department of Civil Engineering, Jubail University College, Royal Commission of Jubail and Yanbu, Jubail, Saudi Arabia*
[6] *UTM Construction Research Centre, Faculty of Civil Engineering, Institute for Smart Infrastructure and Innovative Construction, UTM, Johor Bahru, Johor, Malaysia*
[7] *Facultad de Arquitectura y Urbanismo, Universidad Tecnológica Equinoccial, Calle Rumipamba s/n y Bourgeois, Quito, Ecuador*

Abstract. A perforated shear connector group is commonly used to transfer shear in steel–concrete composite structures when the traditional shear stud connection is not strong enough. The multi-hole perforated shear connector demonstrates a more complicated behavior than the single connector. The internal force distribution in a specific multi-hole perforated shear connector group has not been thoroughly studied. This study focuses on the load-carrying capacity and shear force distribution of multi-hole perforated shear connectors in steel–concrete composite structures. ANSYS is used to develop a three-dimensional finite element model to simulate the behavior of multi-hole perforated connectors. Material and geometric nonlinearities are considered in the model to identify the failure modes, ultimate strength, and load–slip behavior of the connection. A three-layer model is introduced and a closed-form solution for the shear force distribution is developed to facilitate design calculations. The shear force distribution curve of the multi-hole shear connector is catenary, and the efficiency coefficient must be considered in different limit states.

Keywords: steel-concrete structure; perforated shear connector; numerical simulation; mechanical model; efficiency coefficient

1. Introduction

When steel and reinforced concrete are used separately they present some shortcomings and those shortcomings may increase the cost of the construction. For example, steel girders are fabricated using thin plates and as a result of that they are prone to local and lateral buckling as well as fatigue (Andalib *et al.* 2010, Bazzaz *et al.* 2015). Also, the concrete sections are generally thick and unlikely to buckle. However, unlike their high strength in compression they present weak behaviour when they are subjected to tension (Andalib *et al.* 2014, Talaiekhozani *et al.* 2014). Combination of both the steel and concrete in steel-concrete composite beam helps to get the advantages of both.

Modern steel–concrete composite structures are widely used in tall buildings and long bridges. Steel provides resistance to tension forces, while concrete resists compression, provides confinement, and protects the steel from fire.Shear connections are common in steel–concrete composite structures and often control the strength and stiffness of a composite structure.

Shear connection design is an essential part of a steel–concrete composite structure design. The performance of a steel–concrete composite structure can be enhanced by including new shear transfer details at the concrete and steel interface, such as the perforated connection detail that will be discussed in this study.

Since the 1940s, different types of shear connectors have been used in composite structures, such as studs (Viest 1956), high-strength bolts (Dedic and Klaiber 1984), channels (Shariati *et al.* 2010, 2011a, b, c, 2012a, b c, 2016, Baran and Topkaya 2014, Toghroli *et al.* 2014, Shahabi *et al.* 2016), angles (Shariati *et al.* 2012a, 2014a, b), Perforated connectors (Costa-Neves *et al.* 2013), T-perforated connectors (Vianna *et al.* 2008), and bonding connections (Meaud *et al.* 2014). The stud connector is the most widely used shear connector because of its high degree of automation in construction. However, this material can develop cracks in the concrete material and has poor fatigue resistance.

The perforated rib shear connector, which comprises a

---

*Corresponding author, Ph.D.,
E-mail: shariati@tabrizu.ac.ir
**Corresponding author, Ph.D.,
E-mail: zand@iaut.ac.ir
[a] Ph.D.
[b] Ph.D.
[c] Ph.D.
[d] Ph.D. Student
[e] Ph.D.
[f] Ph.D.
[g] Ph.D. Student

steel plate with several uniformly spaced holes, was introduced by (Leonhardt *et al.* 1987). The holes in the perforated steel rib are filled with concrete that forms concrete dowels to provide longitudinal shear resistance. The perforated connector is a popular alternative for applications with high demands for shear capacity, ductility, and fatigue resistance. The performance of perforated connectors has attracted increasing research attention over the past few years, and different methods for calculating connection capacity have been proposed based on push-out tests (e.g., Veldanda and Hosain 1992, Oguejiofor and Hosain 1994, Medberry and Shahrooz 2002, Kim *et al.* 2006, Maleki and Bagheri 2008, Maleki and Mahoutian 2009, Cândido-Martins *et al.* 2010, Costa-Neves *et al.* 2013, Khorramian *et al.* 2015, Tahmasbi *et al.* 2016). Some numerical studies have also investigated the behavior of perforated connectors with different design configurations and loading conditions. Given the complexity of the 3D stress–strain state and the interaction between shear connector and concrete, many researchers, such as (Kraus and Wurzer 1997, Oguejiofor and Hosain 1997, Kim *et al.* 2001, Al-Darzi *et al.* 2007, Bazzaz *et al.* 2014, 2015b) have conducted complicated 3D finite element (FE) simulations to predict the nonlinear response and ultimate load capacity of the connection. These studies used generalized FEM software packages to model the perforated connection to a different level of details. These models must be calibrated and are generally used for research purposes. A simple load capacity model for perforated connections is yet to be developed, thereby providing the impetus of the present study.

Steel–concrete composite action is generally achieved through the load transfer of a series of shear connectors. Compared to single-hole perforated connection, the behavior of multi-hole perforated connection is very complicated because the system is highly indeterminate under loading and each connector is loaded differently according to their location and stiffness. From a connection design perspective, the force transfer mechanism of multi-hole perforated connectors must be examined, and a tractable relationship between single-hole and multi-hole perforated connectors must be established. In this paper, a 3D FE model based on a push-out test specimen was developed through ANSYS to simulate the behavior of multi-hole perforated connectors. Material and geometric nonlinearities were considered in the model to identify the failure modes, ultimate strength, and load–slip behavior of the connection. The model was used to study the internal force transfer mechanism of multi-hole perforated connectors and propose a new "effectiveness factor" for the design of the perforated connector group. A three-layer model was also introduced, and the closed-form solutions of the force distribution and connector reduction factors were investigated.

2. Three-dimensional FEM model

2.1 Finite element model

The general FE analysis software ANSYS was used to

(a) Single-hole perforated   (b) Three-hole perforated   (c) Six-hole perforated
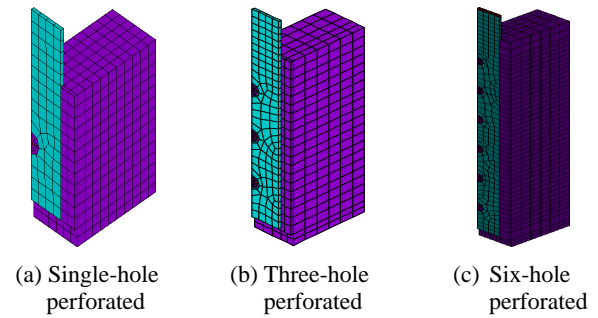
Fig. 1 Three-dimensional FE models

conduct the 3D model analysis. Two types of solid elements in the ANSYS element library were used to model the push-out test specimen. SOLID45 was used for the steel plate modeling and transverse reinforcement. The element was defined by eight nodes, with each node having three translational degrees of freedom. The plasticity capability of the element was enabled in the analyses to model the yielding of steel. Concrete was modeled using the 3D solid element SOLID65, which specializes in modeling reinforced concrete. Link8 element was used to simulate the hooping reinforcement in the test specimen. Surface-to-surface "contact pair" element (CONTA-173 and TARGE170) was used to model the nonlinear behavior of the interface surface between the concrete and steel member.

Fig. 1 shows the FE models of three typical push-out specimens, including single-hole, three-hole, and six-hole perforated connectors, built using ANSYS. Each model comprised four parts, including a concrete block, steel perforated plate, penetrating reinforcement, and hooping. The circular perforated holes on the steel plate had a 60 mm diameter, the steel plate had a thickness of 20 mm, and the steel reinforcement had a diameter of 25 mm. Based on symmetry, only a fourth of the specimens was modeled to reduce the model size. Therefore, the dimensions of the three FE models were set to $400 \times 160 \times 300$, $800 \times 160 \times 300$, and $1400 \times 160 \times 300$ mm, respectively.

2.2 Material modeling

Steel was treated as an ideal elastic-plastic material in the models. As shown in Fig. 2, a bilinear curve was used to model the stress–strain relationship. The behavior in both tension and compression was assumed to be similar. The elastic modulus was $Es = 210$ GPa, and the yield stress was $fys = 345$ MPa. The isotropic material model was used following the von Mises yield criterion.

The concrete was initially assumed as homogeneous. To consider the inelastic behavior of the concrete material, the stress–strain relation proposed by Hognestad (1951) was adopted.

The compressive uniaxial stress–strain relationship for the concrete model was represented by the equations below. Given that the degrading portion of the concrete material could not be incorporated in the ANSYS material nonlinearity, the plastic behavior was adopted after the strain reached $\varepsilon 0$. The stress–strain curve for the concrete is shown in Fig. 2(b).
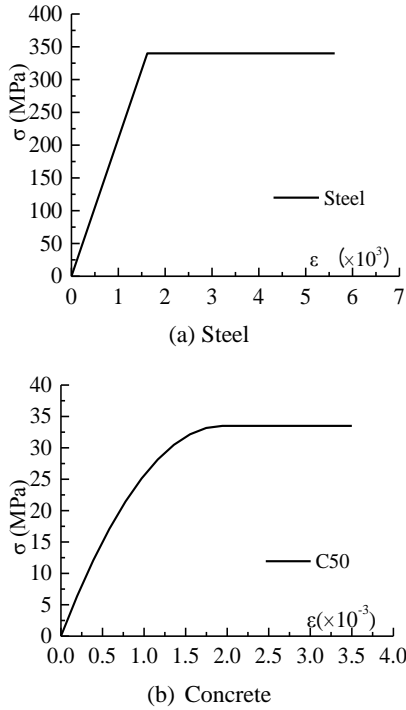
(a) Steel

(b) Concrete

Fig. 2 Stress–strain curve

$$\sigma = 0.85\acute{f_c}[1 - (1 - \varepsilon/\varepsilon_0)^2] \qquad 0 < \varepsilon < \varepsilon 0 \qquad (1)$$

and

$$\sigma = 0.85\acute{f_c}, \quad \varepsilon 0 < \varepsilon < \varepsilon u, \qquad (2)$$

where $\acute{f_c}$ is the compressive cylinder strength of the concrete, $\varepsilon 0 = 1.7 \; \acute{f_c}/E_c$, $\varepsilon u = 0.003$, and Ec is the modulus of elasticity for the concrete.

The behavior in tension was linear with a slope of Ec up to the tensile strength of concrete ft.

2.3 Boundary conditions and loading

The boundary condition of the model was applied based on symmetry condition. All nodes in the lower surface of the concrete block were restricted to resist the compression load. Displacement control was applied to solve the convergence problem in tracking the whole loading process.

3. Three dimensional FEM analyses and validation

The load–slip curve could be plotted and the ultimate capacity could be determined after the analysis. Fig. 3 compares the numerical model simulation for a single-hole perforated connector with the three push-out tests of the single-hole specimen. The FEM results are generally in agreement with those of the push-out test. Although the test was not conducted for three- or six-hole specimens, the calibrated modeling parameters from the single-hole test were used to construct the three- and six-hole models. The behavior of these models, including the crack patterns on the concrete and transverse reinforcement performance, was studied using FEM simulation.
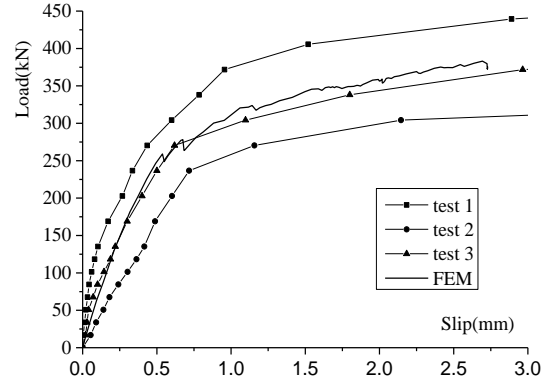

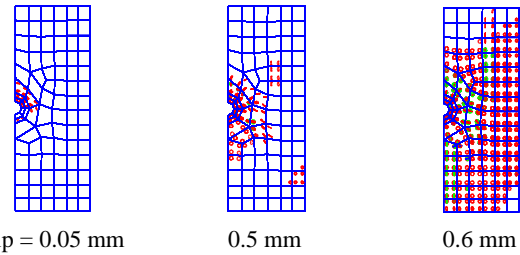Fig. 3 Load–slip curves of single-hole perforated connectors

Slip = 0.05 mm   0.5 mm   0.6 mm

Fig. 4 Crack patterns of single-hole connector specimens

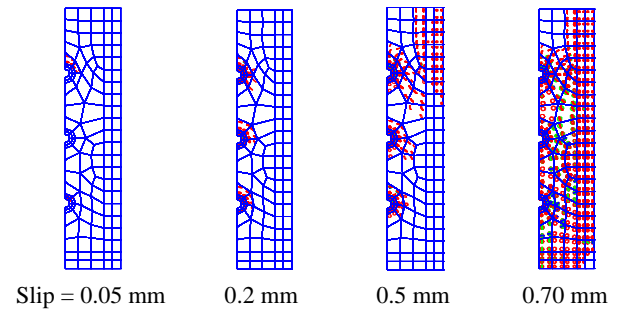Slip = 0.05 mm   0.2 mm   0.5 mm   0.70 mm

Fig. 5 Crack patterns of three-hole connector specimens

3.1 Crack patterns on the concrete

The simulated concrete crack pattern of the single-hole connector specimen was similar to that observed in the test. As shown in Fig. 4, the cracks initially formed near the concrete dowel at the 0.05 mm slip because of stress concentration. When the slip reached 0.6 mm, cracks were formed on the upper and side surfaces of the concrete, while the number and width of these cracks increased until the peak load was reached.

The crack patterns in Fig. 5 demonstrate the failure process of the three-hole connector specimen. These cracks were initially formed near the first and third rows of the concrete dowel at the slip of 0.05 mm. More cracks gradually propagated around each concrete dowel along with an increasing slip. These cracks extended to the upper and side surfaces of the concrete when the slip approached 0.5 mm. Ultimate shear capacity was observed with increasing slip and crack propagation.

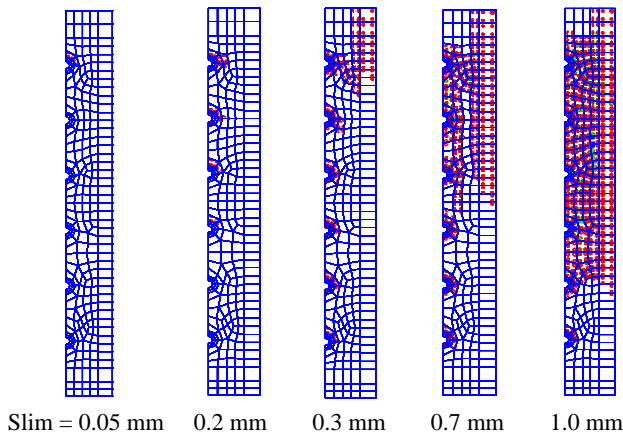Fig. 6 shows the failure process of the six-hole

Fig. 6 Crack patterns of the six-hole connector specimens

Slim = 0.05 mm 0.2 mm 0.3 mm 0.7 mm 1.0 mm

Fig. 9 Stress and slip on the reinforcement

connector specimen under push-out loading. Cracks initially formed near the first row of the concrete dowel at the slip of 0.05 mm. More cracks gradually propagated around each concrete dowel as the applied load was increased. These cracks reached the upper and side surfaces of the concrete when the slip approached 0.3 mm, and the width and number of these cracks continued to increase until the peak load was reached.
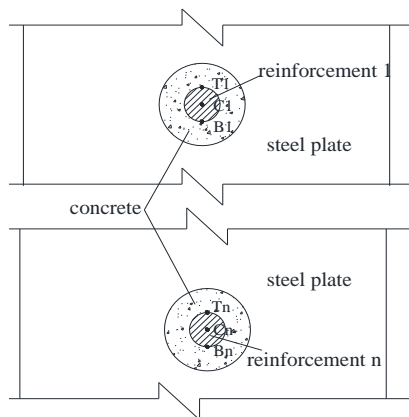
3.2 Behavior of transverse reinforcement

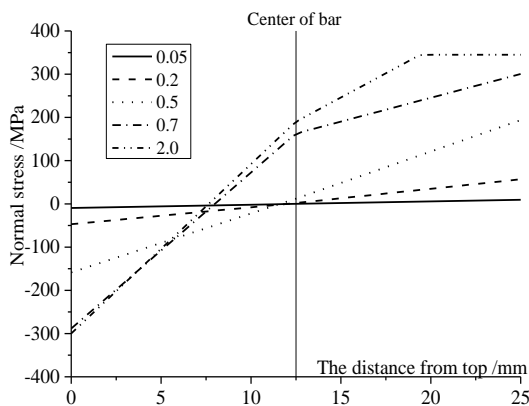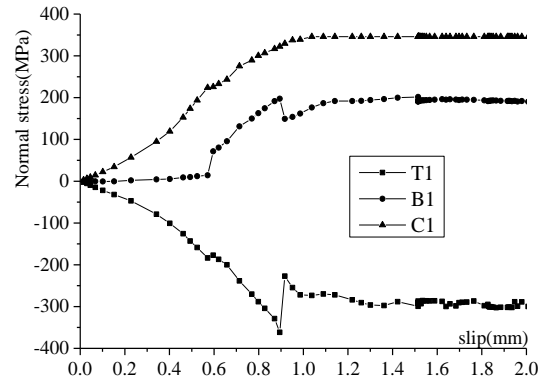Fig. 7 Typical stress points on the reinforcement

Transverse reinforcement typically involves the installation of steel bars through perforated holes and has an important role in transferring load to perforated connectors. To investigate the force transfer mechanism of multi-hole specimens in the push-out test, the stress results on three points located on the top, center, and bottom of each reinforcement section were analyzed. These stress points are shown in Fig. 7.

The simulated normal stresses along the symmetry axis of the middle section of the reinforcement in the single-hole connector specimen are plotted in Fig. 8 under various relative slips. Fig. 9 shows the normal stress–slip curves on the top (T1), center (C1), and bottom (B1) points of the reinforcement. During the push-out test, transverse reinforcement initially transferred load through bending and shear (when the relative slip was less than 0.5 mm), and a small stress occurred on the center of the reinforcement.

When the relative slip reached 0.9 mm, the top and bottom edges of the transverse reinforcement began to yield, while the axial force started to increase in order to transfer those loads with increasing tensile zones on the reinforcement section.

Fig. 10 shows the normal stresses along the symmetry axis of the middle section of all reinforcements in the three-hole connector specimen. Fig. 11 shows the normal stress–slip curves on various points of the transverse reinforcement.

Under push-out loading, the transverse reinforcement suffered from different loads in various rows. When the
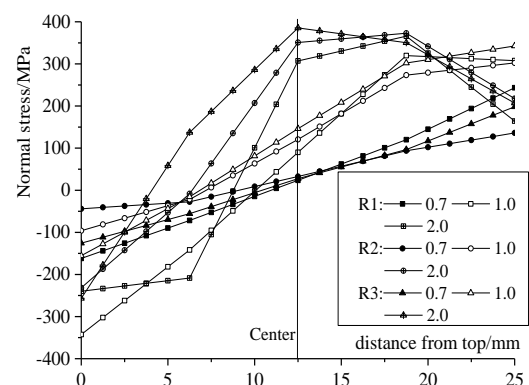
Fig. 8 Stress on the reinforcement section
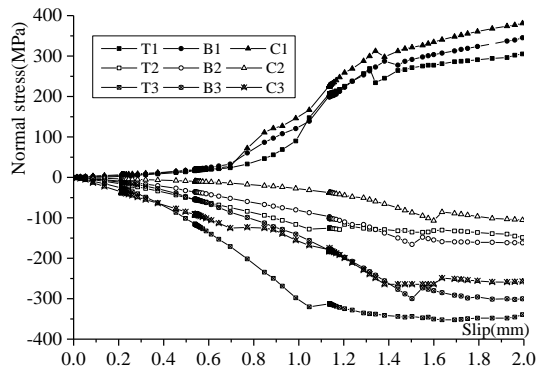
Fig. 10 Stress distribution on the symmetry axis

Fig. 11 Stress and slip on different points
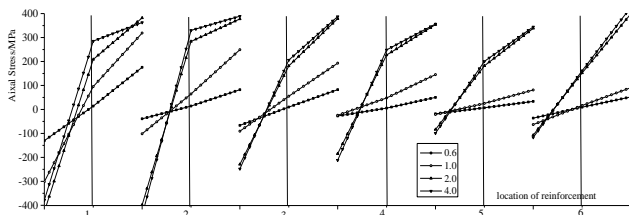
Fig. 12 Normal stress at the middle point of the reinforcement at different locations

(a) Stress on the top point

(b) Stress on the bottom point

Fig. 13 Stress and slip in the transverse reinforcement

relative slip was less than 0.7 mm, the transverse reinforcement mainly bore a bending moment, whereas the normal and shear stresses increased linearly with the slip. Afterward, the normal stress–slip curve of the center point of the reinforcement shows that the axial force began to increase along with the loading. When the relative slip neared 1.0 mm, the transverse reinforcement in the top row began to yield. As the push-out load continued to increase, the plastic zone in the top row of the reinforcement was enlarged, whereas the normal and shear stresses in the other rows of the reinforcement were increased.
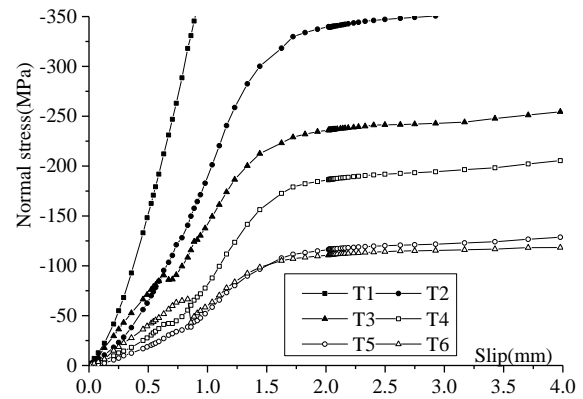
Fig. 12 shows the normal stresses on the symmetry axis of different reinforcements in the six-hole connector specimen. Fig. 13 shows the stress–slip curves on the top and bottom points of the reinforcement.

Obviously, the stresses on each point of the reinforcement were different under push-out loading. The reinforcement was usually located far from the loading end for a smaller force to act upon the reinforcement. When the relative slip was less than 0.6 mm, the normal stress on the reinforcement increased linearly with an increasing slip.
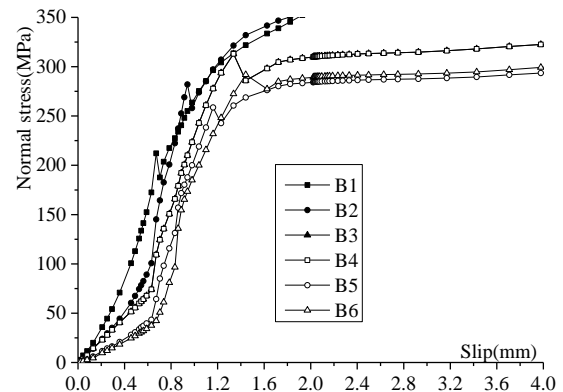
In contrast, when the relative slip was near 1.0 mm, the axial force began to increase and the transverse reinforcement in the top row began to yield. When the load continued to increase, the plastic zone in the top row of the reinforcement was enlarged and the normal stresses in the other rows were increased.

4. Shear force distribution in multi-hole perforated connection

For a multi-hole perforated connection design, one must investigate how the shear transfer mechanism at each row

of connectors changes along with different connection designs. As an indeterminate structural system, the shear force distribution among shear connectors in a multi-hole perforated connection relies on the relative slip at each connector location. On the basis of the FEM results of the multi-hole specimen, the percentage of shear force (relative to total shear load) that acts upon each row of the shear connector under different relative slips are shown in Fig. 14.

Fig. 14 shows that the shear force distribution between each row in the multi-hole perforated shear connector depends on the connection design. The end rows of the multi-hole perforated shear connector generally resist a larger portion of the load.

Given that the connection load–slip curves of three perforated connectors can be simulated (as shown in Fig. 15(a)), the load–slip curves of an equivalent single connector can be obtained by simply dividing the total load by the number of connectors (as shown in Fig. 15(b)). The equivalent single connector must be developed to facilitate the design of multi-hole groups. Similar to the design of eccentric bolt connections in steel, the strength of the entire connector can simply be calculated by the number of connectors multiplied by the capacity of the equivalent single connector. In other words, the strength of multi-hole perforated connectors cannot be calculated by simply multiplying the single connector strength with the total number of connectors.
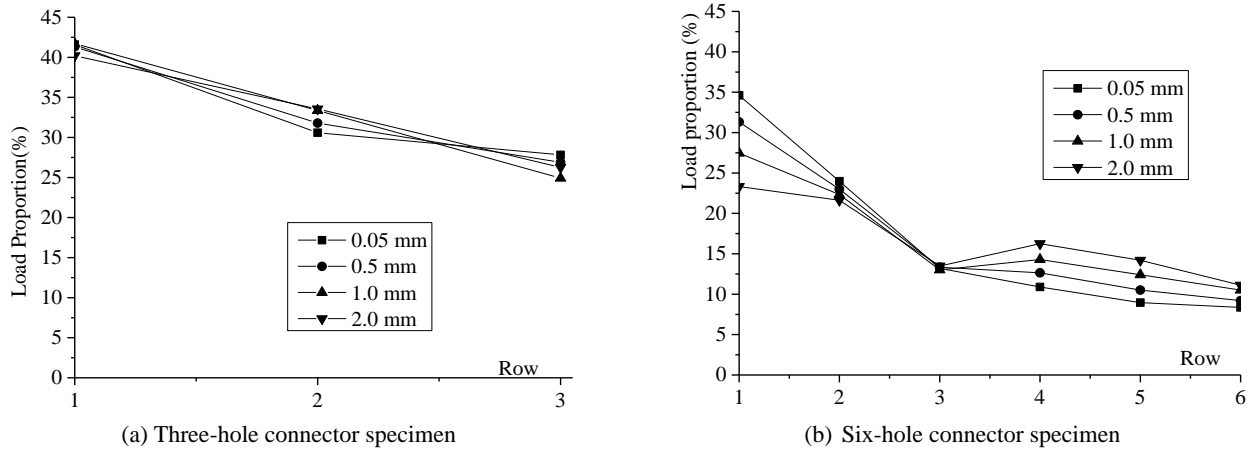
(a) Three-hole connector specimen   (b) Six-hole connector specimen

Fig. 14 Percentage of shear force in each row of the shear connector

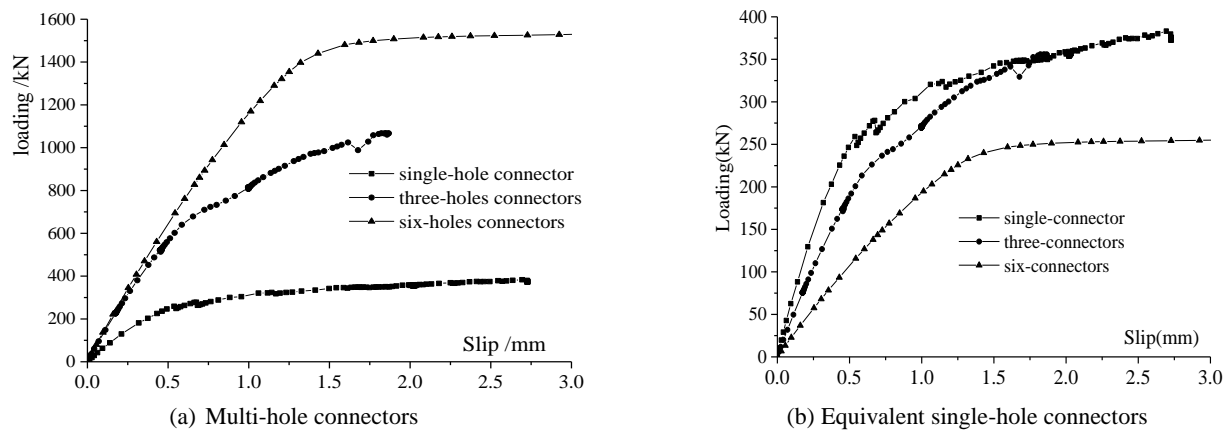(a) Multi-hole connectors   (b) Equivalent single-hole connectors

Fig. 15 Load–slip curves of perforated connectors

This calculation will overestimate the connector strength and produce a non-conservative result. An equivalent strength reduction factor can be obtained through FEM analysis to help simplify the design of a connector group by using single-connector test data.

The reduction factor for different connection design configurations can be determined through the 3D FEM analysis described above. However, the FEM approach is complicated and impractical for design engineers. An analytical solution for the multi-hole perforated connection problem can be derived based on basic design configurations and material properties.

5. Analytical solutions

5.1 Layer equivalence methodology

Fundamentally considered a compatibility problem, the multi-hole perforated shear connector can be described using a three-layer model (Fig. 16) that includes concrete, steel, and connector layers. The compatibility of the concrete, steel, and connector can be captured in this model to produce a closed-form solution for the force distribution and connector reduction factors.

5.2 Control equation of the multi-hole perforated connector

Fig. 17 shows a free-body diagram created from the three-layer structure. The steel member is subjected to axial
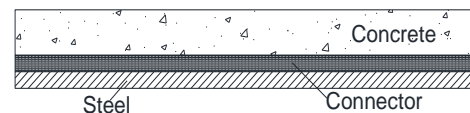

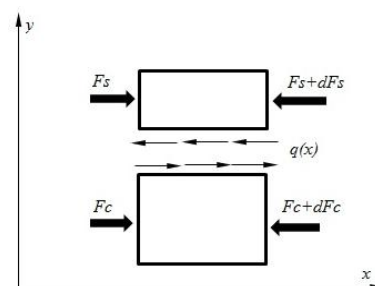Fig. 16 Three-layer structure of the multi-hole perforated shear connector

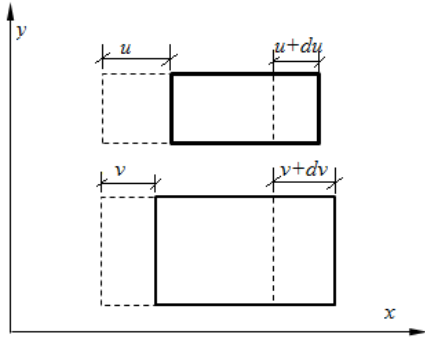Fig. 17 Forces acting upon the free body

Fig. 18 Deformation of the free-body

force F_s and F_s+dF_s at both ends, whereas the concrete member is subjected to the axial force F_c and F_c+dF_c at both ends. Based on the assumed uniform distribution of shear force, a couple of distributed shear force $q(x)$ acts on the interface between the steel and concrete members in opposite directions. Considering the deformation of the free body (Fig. 18), longitudinal deformation u occurs at one end of the steel member and $u+du$ at the other end, whereas longitudinal deformation v occurs at one end of the concrete member and $v+dv$ at the other end.

The general static equilibrium equation can be expressed as follows

$$\begin{cases} F_s(x) - q(x)dx - F_s(x) - dF_s(x) = 0 \\ F_c(x) + q(x)dx - F_c(x) - dF_c(x) = 0 \end{cases} \quad (3)$$

Eq. (1) can be simplified as follows

$$\begin{cases} \dfrac{dF_s(x)}{dx} = -q(x) \\ \dfrac{dF_c(x)}{dx} = q(x) \end{cases} \quad (4)$$

According to linear deformation and strain theory, the relationship between deformation and longitudinal load is expressed

$$\begin{cases} E_s A_s \dfrac{du(x)}{dx} = -F_s(x) \\ E_c A_c \dfrac{dv(x)}{dx} = -F_c(x) \end{cases} \quad (5)$$

Where E_s and E_c denote the modulus of elasticity of steel and concrete respectively, and A_s and A_c denote the representative areas of steel and concrete members respectively.

By substituting Eq. (3) into Eq. (2), we can express the relationship between distributed shear and deformation as

$$\begin{cases} E_s A_s \dfrac{du^2(x)}{dx^2} = -q(x) \\ E_c A_c \dfrac{dv^2(x)}{dx^2} = q(x) \end{cases} \quad (6)$$

Based on the slip–load relationship of the shear connector, the distributed shear $q(x)$ along the x-axis is computed as

$$q(x) = -k(S) \cdot S(x) = -k(S) \cdot [u(x) - v(x)], \quad (7)$$

Where $k(S)$ denotes the shear stiffness of the shear connector, and $S(x)$ denotes the relative slip between the steel and concrete members.

Substituting Eq. (5) into Eq. (4) derives the relationship between relative slip and deformation as

$$\begin{cases} E_s A_s \dfrac{du^2(x)}{dx^2} = k[u(x) - v(x)] = k(S)S(x) \\ E_c A_c \dfrac{dv^2(x)}{dx^2} = -k[u(x) - v(x)] = -k(S)S(x) \end{cases} \quad (8)$$

Subtracting the second formula from the first one can rewrite Eq. (6) as follows

$$\frac{dS^2(x)}{dx^2} - \frac{(E_c A_c + E_s A_s)k(S)}{E_c A_c E_s A_s} S(x) = 0 \quad (9)$$

Shear stiffness $k(S)$ is a nonlinear function of slip that is obtained from the slip–load curve via push-out test. Generally, shear stiffness is defined as a constant when the steel–concrete composite structure is in a normal service condition.

Therefore, differential Eq. (7) can be simplified as follows

$$\ddot{S} - \beta^2 S = 0 \quad (10)$$

Where

$$\beta^2 = \frac{(E_c A_c + E_s A_s)k}{E_c A_c E_s A_s} \quad (11)$$

The general integral of differential Eq. (8) is expressed as

$$S(x) = C_1 e^{\beta x} + C_2 e^{-\beta x}. \quad (12)$$

In the push-out test, the load condition of ends can be defined as follows

$$F_c(x)|_{x=0} = F_s(x)|_{x=l} = 0$$
$$F_c(x)|_{x=l} = F_s(x)|_{x=0} = Q$$

The boundary conditions of differential Eq. (8) can be defined as

$$\begin{cases} \dfrac{dS(x)}{dx}\Big|_{x=0} = \dfrac{du(x) - dv(x)}{dx}\Big|_{x=0} \\ \quad = \dfrac{F_c(x)}{E_c A_c}\Big|_{x=0} - \dfrac{F_s(x)}{E_s A_s}\Big|_{x=0} = -Q \\ \dfrac{dS(x)}{dx}\Big|_{x=l} = \dfrac{du(x) - dv(x)}{dx}\Big|_{x=l} \\ \quad = \dfrac{F_c(x)}{E_c A_c}\Big|_{x=l} - \dfrac{F_s(x)}{E_s A_s}\Big|_{x=l} = Q \end{cases} \quad (13)$$

Differential Eq. (8) can be solved as follows

$$S(x) = \frac{-Q\left(E_c A_c e^{-\beta l} + E_s A_s\right)}{\beta E_s A_s E_c A_c \left(e^{-\beta l} - e^{\beta l}\right)} e^{\beta x}$$
$$+ \frac{-Q\left(E_c A_c e^{\beta l} + E_s A_s\right)}{\beta E_s A_s E_c A_c \left(e^{-\beta l} - e^{\beta l}\right)} e^{-\beta x} \qquad (14)$$

which can be simplified as

$$S(x) = \frac{\varepsilon}{\beta\left(1 - \frac{e^{\beta l} + \gamma}{e^{-\beta l} + \gamma}\right)} e^{\beta x} + \frac{\varepsilon\left(\frac{\gamma + e^{\beta l}}{e^{-\beta l} + \gamma}\right)}{\beta\left(1 - \frac{e^{\beta l} + \gamma}{e^{-\beta l} + \gamma}\right)} e^{-\beta x} \qquad (15)$$

Where

$$\varepsilon = \frac{-Q}{E_s A_s} \quad \text{and} \quad \gamma = \frac{E_s A_s}{E_c A_c}.$$

Given that

$$\xi = \frac{\left(e^{\beta l} + \gamma\right)}{\left(\gamma + e^{-\beta l}\right)}, \quad \text{Eq. (13)}$$

Can be further simplified as follows

$$S(x) = \frac{\varepsilon}{\beta(1 - \xi)}\left(e^{\beta x} - \xi e^{-\beta x}\right) \qquad (16)$$

By using coordinate translation, we can express Eq. (14) as

$$S(x) = \frac{2\varepsilon\sqrt{\xi}}{\beta(1-\xi)} csh\left[\beta\left(x - \frac{ln\xi}{2\beta}\right)\right]. \qquad (17)$$

The shear of every connector can be expressed as follows

$$Q(x) = \int_{x-\frac{d}{2}}^{x+\frac{d}{2}} k\,S(x)dx$$
$$= \frac{2\varepsilon\sqrt{\xi}}{\beta^2(1-\xi)}\left\{sh\left[\beta\left(x - \frac{ln\xi}{2\beta} + \frac{d}{2}\right)\right] \qquad (18)\right.$$
$$\left. - sh\left[\beta\left(x - \frac{ln\xi}{2\beta} - \frac{d}{2}\right)\right]\right\}$$

where d denotes the distance between connectors.

The total shear of connectors can be computed as follows

$$Q(x) = \int_0^l k\,S(x)dx$$
$$= \frac{2\varepsilon k\sqrt{\xi}}{\beta^2(1-\xi)}\left\{sh\left[\beta\left(l - \frac{ln\xi}{2\beta}\right)\right] - sh\left[\beta\left(-\frac{ln\xi}{2\beta}\right)\right]\right\}. \qquad (19)$$

Slip is determined by the character coefficients ε, β, and ξ. ε is the strain of steel member. β is related to the stiffness of the shear connector, steel member, and concrete member, while comprehensive coefficient ξ is related to the stiffness ratio of steel and concrete members γ, the length of the multi-hole perforated shear connector l, and β. Based on Eq. (15), the slip is changed along the x-axis in the multi-hole perforated connection. The shear force is non-uniform

because the shear force distribution depends on the relative slip at each connector location.

The behavior of the multi-hole perforated shear connector changes along with increasing load. These changes can be divided into three phases, namely, elastic stage, single-end plastic stage, and both ends plastic stage.

5.3 Plastic behaviors

When the plastic zone is located only in one end, $S0$ is assumed as the maximum slip of the connector in the elastic stage. When the length of the plastic zone is $a = 0$, the slip in one end is expressed as

$$S(x)x = 0 = S0. \qquad (20)$$

Substituting $x = 0$ into Eq. (15) obtains the following expression

$$\frac{2\varepsilon\sqrt{\xi}}{\beta(1-\xi)} csh\left[\beta\left(-\frac{ln\xi}{2\beta}\right)\right] = S_0 \qquad (21)$$

As defined forward $\varepsilon = \frac{-Q}{E_s A_s}$, the total shear force can be obtained as

$$Q = \frac{S_0 E_s A_s \beta(\xi - 1)}{(1 + \xi)} \qquad (22)$$

When the length of the plastic zone is $a > 0$, the following boundary conditions are assumed

$$S(x)x = 0 = S0, \quad S(\dot{x})|_{x=0} = \frac{-Q + kS_0 a(1+\gamma)}{E_s A_s}, \quad \text{and}$$
$$S(\dot{x})|_{x=l-a} = \frac{Q}{E_c A_c}.$$

Substituting these boundary conditions into Eq. (10) yields the following equation

$$S(x) = \left(\frac{S_0}{2} + \frac{kS_0 a(1+\gamma) - Q}{2E_s A_s \beta}\right) e^{\beta x}$$
$$+ \left(\frac{S_0}{2} - \frac{kS_0 a(1+\gamma) - Q}{2E_s A_s \beta}\right) e^{-\beta x}. \qquad (23)$$

The length of the plastic zone a can be calculated as follows

$$\frac{Q}{E_s A_s \beta S_0} = \frac{\left(e^{2\beta l} - e^{2\beta a}\right) + kS_0 a(1+\gamma)\left(e^{2\beta l} + e^{2\beta a}\right)}{\left(2\gamma e^{\beta(l+a)} + e^{2\beta a} + e^{2\beta l}\right)} (24)$$

The length of the plastic zone increases in one end along with an increasing load until the slip in the other end reaches the maximum elastic slip $S0$. The slip distribution equation of the elastic section is presented as follows

$$S(x) = C_1 csh[\beta(x - C_2)] \qquad (25)$$

When the length of the plastic zone is a=a0, the following boundary conditions are assumed

When $x = 0$ or $x = 1 - a0$, $S(x) = S0$.

On the basis of Eq. (11), the following boundary conditions are obtained

$$S(\dot{x})|_{x=0} = \frac{-Q + kS_0 a_0 (1 + \gamma)}{E_s A_s}$$

and

$$S(\dot{x})|_{x=l-a_0} = \frac{Q}{E_c A_c}.$$

By substituting these boundary conditions into Eq. (23), we obtain the following

$$S(x) = \frac{S_0}{csh[\beta((l - a_0)/2)]} csh[\beta(x - (l - a_0)/2)] \quad (26)$$

$$Q = \frac{a_0 k S_0 (1 + \gamma)}{(1 - \gamma)} \quad (27)$$

The length of the plastic zone a0 can be calculated as

$$a_0 = \frac{E_c A_c \beta}{k} \cdot \frac{sh\left[\beta\left(\frac{l-a_0}{2}\right)\right]}{csh\left[\beta\left(\frac{l-a_0}{2}\right)\right]} \cdot \frac{(1 - \gamma)}{(1 + \gamma)}$$

$$= \frac{E_c A_c \beta}{k} \cdot \frac{e^{\beta l} - e^{\beta a_0}}{e^{\beta l} + e^{\beta a_0}} \cdot \frac{(1 - \gamma)}{(1 + \gamma)}. \quad (28)$$

When the length of the plastic zone in one end is a>a0 and the length of the elastic section is b, the length of the plastic zone in the other end is l-b-a.

$$S(x) = C_1 csh[\beta(x - C_2)]$$

Boundary conditions

$$S(x)x = 0 = S0, \qquad S(x)x = b = S0$$

$$S(\dot{x})|_{x=0} = \frac{-Q + kS_0 a(1+\gamma)}{E_s A_s}, \text{ and}$$

$$S(\dot{x})|_{x=b} = \frac{\gamma Q - kS_0(l-b-a)(1+\gamma)}{E_s A_s}.$$

The following equations are obtained when these boundary conditions are substituted into Eq. (23)

$$b = l - \frac{Q}{kS_0} + \frac{2}{\beta} \frac{sh(\beta b/2)}{csh(\beta b/2)} \quad (29)$$

and

$$a = \frac{l - b}{2} + \frac{Q(1 - \gamma)}{2kS_0(1 + \gamma)} \quad (30)$$

Given that $b = \alpha$l

$$Q = kS_0 l(1 - \alpha) + \frac{2}{\beta} \frac{e^{\beta\alpha l} - 1}{e^{\beta\alpha l} + 1} kS_0 \quad (31)$$

And

$$S(x) = \frac{S_0}{csh(\beta b/2)} csh\left[\beta\left(x - \frac{b}{2}\right)\right] \quad (32)$$

Based on Eq. (17), (20), (25), or (29), the total shear of connectors Q can be determined and the efficiency coefficient η can be expressed as follows

$$\eta = Q/(klS0). \quad (33)$$

Similar to the group factor used to design eccentric steel bolt groups, the above efficiency coefficient can be very useful for designing perforated connections.

5.4 Design example

According to the above analysis, four limit states of multi-hole perforated shear connection must be investigated, including both- and single-edge yields of the connector, steel plate yield, and concrete crushing. Steel plate yield is determined by the cross-section area of the steel plate and the yield strength of the steel material. Concrete crushing is mainly determined by the effective area of the concrete member and the compressive strength of the concrete material.

The ultimate limit state of the multi-hole perforated shear connection is generally defined by the maximum elastic slip according to the loading–slip curve. Fig. 15 shows that the maximum elastic slip of multi-hole perforated shear connections is greater than that of single-hole perforated shear connections. In other words, when the slip of the connector, which bears a maximum shear force, is equivalent to the maximum elastic slip, the multi-hole perforated steel-concrete joint remains elastic and can bear much more load. The single-edge yield of the connector must not be considered as the design limit state of the multi-hole perforated shear connector, while the maximum load of the elastic stage, Q1 (Eq. (20)), must not be defined as design shear resistant.

In $Qs = fs.As$, Qs is the maximum load result in the steel plate yield, fs is the yield strength of the steel material, and As is the cross-section area of the steel plate. When Qs is less than $Q2$ (Eq. (25)), the steel plate in the multi-hole perforated shear connection yields before the both-edge yield of the connector. When Qs is greater than $Q2$, the length of the plastic zone and the maximum relative slip must be investigated.

Shear connection was designed in this section to illustrate the design procedure. Table 1 shows the configuration of this connection, which is designed to resist a factored load of 1150 kN. The design process must decide the number of perforated connectors to be included.

The shear resistance of the single-hole perforated shear is expressed as $R1 = K.S0 = 240$ kN. If the shear force distribution is assumed as uniform, then the five-hole perforated shear connection can meet the design requirements. Given the real shear force distribution and yield process of perforated shear connections, when the plastic zone is located only in one end, substituting these character coefficients into Eqs. (20) and (25) can address the total shear force in the single- and two-end yields.

Table 1 Design parameters of the perforated shear connection

Es/GPa	As/m^2	Ec/GPa	Ac/m^2	S0/mm	K kN/m	d/m	Fs/MPa
210	0.0045	35	0.04	0.6	4e+5	0.3	345

Table 2 Shear resistance and efficiency coefficients

Number of holes	Items	Single-end yield	Two-end yield	$\rho = 1/2$	$\rho = 2/3$
5	Shear resistance	754	968	1141	1181
	Efficiency coefficient	0.628	0.807	0951	0.984
6	Shear resistance	797	1070	1343	1408
	Efficiency coefficient	0.553	0.743	0.933	0.978
7	Shear resistance	825	1143	1535	1631
	Efficiency coefficient	0.491	0.680	0.914	0.971
8	Shear resistance	842	1194	1716	1850
	Efficiency coefficient	0.439	0.622	0.894	0.964
9	Shear resistance	853	1228	1888	2063
	Efficiency coefficient	0.395	0.569	0.874	0.955

Owing to the yield ratio (the ratio of plastic zone length and total length) ρ, the total shear resistance Q in different yield ratios can be determined using Eq. (29).

Table 2 lists the shear resistance and efficiency coefficient of perforated shear connections with various numbers of holes. The efficiency coefficient increases along with yield ratio and decreases along with the number of holes.

When the yields of two ends are considered the design limit states, the eight-hole perforated shear connection must be selected. However, for a limit state yield ratio of $\rho = 0.5$, selecting the six-hole perforated shear connection is preferable.

6. Conclusions

This paper investigated the shear force transfer mechanism of multi-hole perforated shear connection for steel–concrete composite structures. On the basis of nonlinear finite element analysis and simplified layer-equivalence methodology, the following conclusions were drawn:

- Crack patterns on the concrete and stress of transverse reinforcement show that non- uniformity of shear force distribution in perforated shear connection cause lower efficiency of shear resistance with the row number increasing.
- Transverse reinforcement has an important role in load-sharing in perforated connectors. The reinforcement tends to bend under a small slip, but the axial force increases along with the slip. The

reinforcement in the top row will be the first to yield.

- The stiffness of the connection increases along with the number of holes. The failure mode of the connection can also change from connector failure to steel plate yielding. The connection capacity increases along with the number of connectors, but is capped by the steel plate yielding limit state.
- Given the uneven distribution of shear force at each row of connectors, an efficiency coefficient must be considered when calculating the connector group strength. A closed-form solution for the efficiency coefficient is derived in this study to be used in connection design.

References

Al-Darzi, S., Chen, A. and Liu, Y. (2007), "Finite element simulation and parametric studies of perfobond rib connector", *Am. J. Appl. Sci.*, **4**(3), 122-127.

Andalib, Z., Kafi, M. and Bazzaz, M. (2010), "Using hyper elastic material for increasing ductility of bracing", *Proceedings of the 1st. Conference of Steel & Structures and 2nd Conference on Application of High-Strength Steels in Structural Industry*, Tehran, Iran, December.

Andalib, Z., Kafi, M.A., Kheyroddin, A. and Bazzaz, M. (2014), "Experimental investigation of the ductility and performance of steel rings constructed from plates", *J. Constr. Steel Res.*, **103**, 77-88.

Baran, E. and Topkaya, C. (2014), "Behavior of steel–concrete partially composite beams with channel type shear connectors", *J. Constr. Steel Res.*, **97**, 69-78.

Bazzaz, M., Kafi, M.A., Kheyroddin, A., Andalib, Z. and Esmaeili, H. (2014), "Evaluating the seismic performance of off-centre bracing system with circular element in optimum place", *Int. J. Steel Struct.*, **14**(2), 293-304.

Bazzaz, M., Andaliba, Z., Kafib, M.A. and Kheyroddin, A. (2015a), "Evaluating the performance of OBS-CO in steel frames under monotonic load", *Earthq. Struct., Int. J.*, **8**(3), 699-712.

Bazzaz, M., Andalib, Z., Kheyroddin, A. and Kafi, M.A. (2015b), "Numerical comparison of the seismic performance of steel rings in off-centre bracing system and diagonal bracing system", *Steel Compos. Struct., Int. J.*, **19**(4), 917-937.

Cândido-Martins, J.P.S., Costa-Neves, L.F. and Vellasco, P.C.G.d.S. (2010), "Experimental evaluation of the structural response of Perfobond shear connectors", *Eng. Struct.*, **32**(8), 1976-1985.

Costa-Neves, L.F., Figueiredo, J.P., Vellasco, P.C.G.d.S. and Vianna, J.d.C. (2013), "Perforated shear connectors on composite girders under monotonic loading: An experimental approach", *Eng. Struct.*, **56**, 721-737.

Dedic, D. and Klaiber, F. (1984), "High-strength bolts as shear connectors in rehabilitation work", *Concrete Int.*, **6**(7), 41-46.

Hognestad, E. (1951), "Study of combined bending and axial load in reinforced concrete members", University of Illinois at Urbana Champaign, College of Engineering; Engineering

Experiment Station.

Khorramian, K., Maleki, S., Shariati, M. and Ramli Sulong, N.H. (2015), "Behavior of tilted angle shear connectors", *PLoS one*, **10**(12), e0144288.

Kim, B. Wright, H. and Cairns, R. (2001), "The behaviour of through-deck welded shear connectors: An experimental and numerical study", *J. Constr. Steel Res.*, **57**(12), 1359-1380.

Kim, H.Y., Jeong Y.J., Kim, T.H. and Park, S.K. (2006), "Structural performance of steel-concrete composite deck for steel-box girder bridges", *KSCE J. Civil Eng.*, **10**(5), 357-363.

Kraus, D. and Wurzer, O. (1997), "Nonlinear finite-element analysis of concrete dowels", *Comput. Struct.*, **64**(5-6), 1271-1279.

Leonhardt, F., Andrä, W., Andrä, H. and Harre, W. (1987), "New advantageous shear connection for composite structures with high fatigue strength", *Beton Stahlbetonbau*, **62**(12), 325-331.

Maleki, S. and Bagheri, S. (2008), "Behavior of channel shear connectors, Part I: Experimental study", *J. Constr. Steel Res.*, **64**, 1333-1340.

Maleki, S. and Mahoutian, M. (2009), "Experimental and analytical study on channel shear connectors in fiber-reinforced concrete", *J. Constr. Steel Res.*, **65**(8-9), 1787-1793.

Meaud, C., Jurkiewiez, B. and Ferrier, E. (2014), "Steel–concrete bonding connection: An experimental study and non-linear finite element analysis", *Int. J. Adhes. Adhes.*, **54**, 131-142.

Medberry, S. and Shahrooz, B. (2002), "Perfobond shear connector for composite construction", *Eng. J.*, **39**(1), 2-12.

Oguejiofor, E. and Hosain, M. (1994), "A parametric study of perfobond rib shear connectors", *Can. J. Civil Eng.*, **21**(4), 614-625.

Oguejiofor, E. and Hosain, M. (1997), "Numerical analysis of push-out specimens with perfobond rib connectors", *Comput. Struct.*, **62**(4), 617-624.

Shahabi, S., Ramli Sulong, N.H., Shariati, M., Mohammadhassani, M. and Shah, S. (2016), "Numerical analysis of channel connectors under fire and a comparison of performance with different types of shear connectors subjected to fire", *Steel Compos. Struct., Int. J.*, **20**(3), 651-669.

Shariati, M., Ramli Sulong, N.H. and Arabnejad Khanouki, M.M. (2010), "Experimental and analytical study on channel shear connectors in light weight aggregate concrete", *Proceedings of the 4th International Conference on Steel & Composite Structures*, Sydney, Australia, July.

Shariati, M., Ramli Sulong, N.H., Sinaei, H., Arabnejad Khanouki, M.M. and Shafigh, P. (2011a), "Behavior of channel shear connectors in normal and light weight aggregate concrete (experimental and analytical study)", *Adv. Mater. Res.*, **168**, 2303-2307.

Shariati, M., Ramli Sulong, N.H., Arabnejad Khanouki, M.M. and Shariati, A. (2011b), "Experimental and numerical investigations of channel shear connectors in high strength concrete", *Proceedings of the 2011 World Congress on Advances in Structural Engineering and Mechanics (ASEM'11+)*, Seoul, South Korea, August 2011.

Shariati, M., Ramli Sulong, N.H., Arabnejad Khanouki, M.M. and Mahoutian, M. (2011c), "Shear resistance of channel shear connectors in plain, reinforced and lightweight concrete", *Sci. Res. Essays*, **6**(4), 977-983.

Shariati, M., Ramli Sulong, N.H., Suhatril, M., Shariati, A., Arabnejad, M.M.K. and Sinaei, H. (2012a), "Behaviour of C-shaped angle shear connectors under monotonic and fully reversed cyclic loading: An experimental study", *Mater. Des.*, **41**, 67-73.

Shariati, M., Ramli Sulong, N.H. and Arabnejad Khanouki, M.M. (2012b), "Experimental assessment of channel shear connectors under monotonic and fully reversed cyclic loading in high strength concrete", *Mater. Des.*, **34**, 325-331.

Shariati, M., Ramli Sulong, N.H., Suhatril, M., Shariati, A., Arabnejad Khanouki, M. and Sinaei, H. (2012c), "Fatigue energy dissipation and failure analysis of channel shear connector embedded in the lightweight aggregate concrete in composite bridge girders", *Proceedings of the Fifth International Conference on Engineering Failure Analysis*, The Hague, The Netherlands, July 2012.

Shariati, A., Ramli Sulong, N.H., Suhatril, M. and Shariati, M. (2012d), "Investigation of channel shear connectors for composite concrete and steel T-beam", *Int. J. Phys. Sci.*, **7**(11), 1828-1831.

Shariati, A., Shariati, M., Ramli Sulong, N.H., Suhatril, M., Arabnejad Khanouki, M.M. and Mahoutian, M. (2014a), "Experimental assessment of angle shear connectors under monotonic and fully reversed cyclic loading in high strength concrete", *Constr. Build. Mater.*, **52**, 276-283.

Shariati, M., Shariati, A., Ramli Sulong, N.H., Suhatril, M. and Khanouki, M.A. (2014b), "Fatigue energy dissipation and failure analysis of angle shear connectors embedded in high strength concrete", *Eng. Fail. Anal.*, **41**, 124-134.

Shariati, M., Ramli Sulong, N.H., Shariati, A. and Kueh, A.B.H. (2016), "Comparative performance of channel and angle shear connectors in high strength concrete composites: An experimental study", *Constr. Build. Mater.*, **120**, 382-392.

Tahmasbi, F., Maleki, S., Shariati, M., Ramli Sulong, N.H. and Tahir, M. (2016), "Shear capacity of C-shaped and L-shaped angle shear connectors", *PloS one*, **11**(8), e0156989.

Talaiekhozani, A., Keyvanfar, A., Andalib, R., Samadi, M., Shafaghat, A., Kamyab, H., Majid, M.Z.A., Zin, R.M., Fulazzaky, M.A., Lee, C.T. and Hussin, M.W. (2014), "Application of *Proteus mirabilis* and *Proteus vulgaris* mixture to design self-healing concrete", *Desal. Water Treat.*, **52**(19-21), 3623-3630.

Toghroli, A., Mohammadhassani, M., Suhatril, M., Shariati, M. and Ibrahim, Z. (2014), "Prediction of shear capacity of channel shear connectors using the ANFIS model", *Steel Compos. Struct., Int. J.*, **17**(5), 623-639.

Veldanda, M. and Hosain, M. (1992), "Behaviour of perfobond rib shear connectors: push-out tests", *Can. J. Civil Eng.*, **19**(1), 1-10.

Vianna, J.d.C., Costa-Neves, L.F., Vellasco, P.C.G.d.S. and de Andrade, S.A.L. (2008), "Structural behaviour of T-Perfobond shear connectors in composite girders: An experimental approach", *Eng. Struct.*, **30**(9), 2381-2391.

Viest, I. (1956), "Investigation of stud shear connectors for composite concrete and steel T-beams", *Journal Proceedings*, **52**(4), 875-892.

CC